



TECHNICAL ARTICLE

# Hot Deformation Behavior of Homogenized Al-7.8Zn-1.65Mg-2.0Cu (wt.%) Alloy

Dao-xiang Wu, Shuai Long, Shi-shan Li, Yu-ting Zhou, Shu-yan Wang, Qing-wei Dai, and Hai-tao Lin

Submitted: 5 November 2021 / Revised: 4 July 2022 / Accepted: 20 July 2022 / Published online: 12 September 2022

The flow curves of Al-7.8Zn-1.65Mg-2.0Cu (wt.%) alloy in the temperature range of 300–450 °C and strain rate range of 0.01–10 s<sup>-1</sup> were obtained by hot compression tests on a Gleeble-3500 isothermal simulator. The effects of deformation heat-induced temperature rising and friction on the flow curves were discussed and the flow curves were corrected to exclude these influences. The constitutive model was constructed and its accuracy was evaluated by the correlation coefficient (*R*) and average absolute relative error. The values of the corresponding evaluators were determined to be 0.9841 and 6.2346%, respectively. The processing maps were developed and through which the optimal hot working window for this alloy was determined in the range of 380–450 °C and 0.01–0.368 s<sup>-1</sup>. The microstructure evolution observations revealed that micro-crack and flow localization occurred at 300 °C and 10 s<sup>-1</sup> and 400 °C and 10 s<sup>-1</sup>, which located in the instability region of processing map. With the increasing strain rate, the deformation activation energy decreased, simultaneously, the dislocation multiplication rate accelerated, which resulted in pronounced increasing of LAGBs and HAGBs.

**Keywords** Al-7.8Zn-1.65Mg-2.0Cu (wt.%) alloy, constitutive model, hot compression, microstructure evolution, processing map

## 1. Introduction

Al-Zn-Mg-Cu series alloys have been widely used in the industrial fields of automotive, aerospace, marine due to the good combination property of high specific strength, high corrosion resistance etc. (Ref 1–3). Forging is one of the most extensively used processing methods of these alloys in manufacturing the structural components in above fields. Before forming a certain forging, processing parameter sets need to be determined and they are usually optimized by finite element simulation and microstructure evolution analysis, which relies on the investigation of hot deformation behavior (Ref 4–7). In regardless of the deformation parameters, hot deformation behavior of an aluminum alloy is mainly affected by its chemical compositions. The proportions of alloying elements bring great difference. For example, Tang et al. (Ref 8) found that with the increasing Zn content of an Al-Zn-Mg-Cu alloy, the strain hardening effect is strengthened and dynamic softening is accelerated at 300 °C but decelerated at 400 °C. Qian et al. (Ref 9) found that the Mn addition influenced the flow behavior of 6082 aluminum alloy obviously

and the apparent activation energy increased with the increasing Mn addition, simultaneously, dynamic recovery (DRV) and dynamic recrystallization (DRX) were inhibited. As for the Al-7.8Zn-1.65Mg-2.0Cu (wt.%) alloy which has different chemical compositions from the existed Al-Zn-Mg-Cu alloys, the former researches can offer little reference to the new forging development, thus it is necessary to investigate its hot deformation behavior.

Isothermal compression test has been extensively used to study the hot deformation behavior of alloys. Based on that, Li et al. (Ref 10) studied the hot deformation and dynamic recrystallization behavior of Al-Si-Mg alloy, they calculated the Zener-Hollomon value through stress–strain data and discussed the relationship between this value and different DRX mechanisms. Rudra et al. (Ref 11) developed the constitutive model of a SiC particle strengthened Al-5083 composite on the basis of stress–strain curves. They compared the prediction precision between modified Johnson-Cook model and modified Zeller-Armstrong model and found the later one better. However, the aforementioned reports took no consideration of the effect of temperature rising induced by deformation heat and friction between anvils and specimens on the flow stress during compression tests. This effect has been proved to affect flow stress pronouncedly (Ref 12) and it was discussed by few investigation. For instance, Hao et al. (Ref 13) corrected the flow stress of 7A21 alloy by excluding the effect of temperature rise induced by deformation heat and friction through the methods proposed by Geotz et al. (Ref 14) and Ebrahimi et al. (Ref 15). The results show that the friction increases the flow stress and temperature rising reduces the flow stress, respectively. Hence, to accurately understand the flow behavior of the investigated alloy, it is important to correct the flow stress by excluding the effects of temperature rising and friction.

Constitutive models including Johnson-Cook model, Zerilli-Armstrong model, Hansel-Spittle model and Arrhenius model describe the flow stress by mathematic formulas, which are the

Dao-xiang Wu, Shu-yan Wang, and Hai-tao Lin, Southwest Aluminum Group Co. Ltd, Chongqing 401326, China; Shuai Long and Qing-wei Dai, College of Metallurgy and Material Engineering, Chongqing University of Science and Technology, Chongqing 400331, China; and Shi-shan Li and Yu-ting Zhou, College of Materials Science and Engineering, Chongqing University, Chongqing 400044, China. Contact e-mail: longshuai@cqust.edu.cn.

bases of finite element simulation. Among these models, strain compensated Arrhenius model has been applied on lead alloy (Ref 16-18), titanium alloy (Ref 19), magnesium alloy (Ref 20) and aluminum alloy (Ref 13). It has been proved to be sufficiently precise compared with other models in the many researches (Ref 21-23). As mentioned above, the flow behavior changes with the variation of chemical compositions, for this novel Al-7.8Zn-1.65Mg-2.0Cu (wt.%) alloy, it is quite important to construct the constitutive relationship by the precise strain compensated Arrhenius model to better understand the flow behavior. Besides, the investigation of microstructure evolution under different deformation conditions is also very valuable, it helps to figure out the intrinsic hot workabilities of alloys. Processing map combines the deformation parameters with the microstructures, it is derived from the dynamic materials model. The most widely used processing map is based on the criterion proposed by Prasad et al. (Ref 24, 25). Its application combined with microstructure analysis in titanium alloy (Ref 19, 26), magnesium alloy (Ref 27), aluminum alloy (Ref 28) and steel alloy (Ref 29) have proven that it is mature in unveiling the optimal hot working windows of alloys. However, this work has not been reported previously for this alloy. Thus, constructing the constitutive model and processing map based on corrected flow stress, are the keys to reveal the exact flow behavior and the intrinsic hot workability of this novel alloy, which will offer great references for the process design.

In this work, the isothermal compression tests were conducted on a Gleeble-3500 isothermal simulator to obtain the flow curves of homogeneous Al-7.8Zn-1.65Mg-2.0Cu (wt.%) alloy. The flow curves were then corrected to exclude the effects of deformation heat and friction. Based on the flow stress, the strain compensated Arrhenius model and processing map were constructed. The microstructure evolution of this alloy was analyzed by optical microscopy (OM) and electron back-scattered diffraction (EBSD). Finally, the hot deformation behavior was achieved and the optimal hot working window was identified.

## 2. Experimental

### 2.1 Compression Tests

The specimens were machined from the homogenized Al-7.8Zn-1.65Mg-2.0Cu (wt.%) alloy (chemical compositions of (wt.%): Fe-0.04, Zn-7.80, Cr-0.02, Mg-1.65, Mn-0.02, Cu-2.00, Zr-0.10, Si-0.03, Ti-0.03, and the balance of Al, initial OM microstructure is shown in Fig. 1) billet into cylinders with diameters of 8 mm and heights of 12 mm. The two end faces of the specimens were ground by sandpapers to reduce the effect of friction on the experimental results. The hot compression tests were conducted on a Gleeble-3500 isothermal simulator at the temperatures of 300, 350, 400, 450 °C and the strain rates of 0.01, 0.1, 1, 10 s<sup>-1</sup> with the height reduction of 60%. Before compression, graphite flakes were inserted between anvils and the end faces of specimens to furtherly reduce the effect of friction. Meanwhile, the specimens were heated by 5 °C/s to the certain temperatures and hold 180 s to obtain uniform temperature distribution. During compression, the true stress-strain curves were obtained automatically by the equipped monitor.

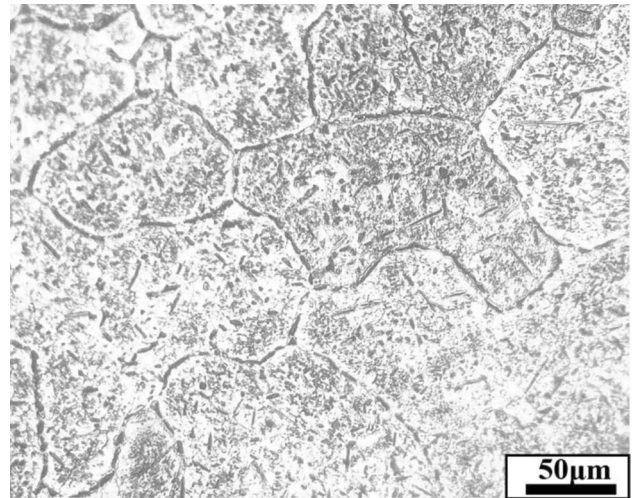


Fig. 1 Initial microstructure of the tested alloy

### 2.2 Preparation for Microstructure Analysis

The specimens were quenched in cold water immediately after compression and then cut along the compressive direction across their centers by wire-electrode cutting method. The cutting faces then were ground by sandpapers with granularities of #200-#4000. The specimens for optical microscopy (OM) observation were then mechanical polished and etched by the Keller solution (H<sub>2</sub>O:HNO<sub>3</sub>:HCl:HF = 95 mL:2.5 mL:1.5 mL:1 mL). The specimens for electron back-scattered diffraction (EBSD) characterization were electro-chemical polished in the solution of HNO<sub>3</sub>:CH<sub>3</sub>OH = 30 mL:70 mL at the temperature of -30 °C for 30 s after grinding. The microstructure observation area is at the geometric center of the cutting face.

## 3. Results and Discussion

### 3.1 Flow Curves and Corrections

**3.1.1 Temperature Correction.** It is well-known that the temperature of the specimen will be elevated due to the deformation heat, especially at higher strain rate. The temperature rise of the specimen will lead to reduction of flow stress, which will cause the measured flow stress inaccurate. To correct the flow stress, R.L. Goetz (Ref 14) proposed a correction equation as shown in Eq 1.

$$\Delta T = (0.95\eta \int \sigma d\varepsilon) / (\rho C_p) \quad (\text{Eq 1})$$

where  $\Delta T$  is temperature rise (°C),  $\sigma$  is flow stress (MPa),  $\varepsilon$  is true strain,  $\rho$  is density (g/cm<sup>3</sup>),  $C_p$  is heat capacity (J/gK),  $\eta$  is adiabatic correction coefficient which is related to the strain rate according the following expression:

$$\eta = \begin{cases} 0 & \dot{\varepsilon} \leq 0.001\text{s}^{-1} \\ 0.316 \log_{10} \dot{\varepsilon} + 0.95 & 0.001\text{s}^{-1} < \dot{\varepsilon} < 1\text{s}^{-1} \\ 0.95 & \dot{\varepsilon} \geq 1\text{s}^{-1} \end{cases} \quad (\text{Eq 2})$$

The values of heat capacity (J/gK) and density (g/cm<sup>3</sup>) of the Al-Zn-Mg-Cu alloy can be linearly interpolated from the results reported by Pu et al. (Ref 30) and listed in Table 1.

After the temperature rise value determined ( $\Delta T$ ), the stress softening value ( $\Delta\sigma$ ) can be calculated according to the following equation proposed by Gholamzadeh et al. (Ref 31). Then the temperature corrected flow stress can be obtained as shown in Fig. 2.

$$\Delta\sigma = \Delta T \left. \frac{d\sigma}{dT} \right|_{\epsilon, \dot{\epsilon}} \quad (\text{Eq 3})$$

**3.1.2 Friction Correction.** It is known that even if the cutting board and the end faces of the specimens were padded with graphite flakes, the whole hot compression process is still affected by the friction between the two contact surfaces, and

**Table 1 The linear interpolated density and heat capacity of Al-Zn-Mg-Cu alloy**

Temperature, °C	300	350	400	450
Density, g/cm <sup>3</sup>	2.74	2.727	2.713	2.699
Heat capacity, J/(gK)	0.982	0.994	1.01	1.026

the influence will be reflected in the true stress–strain curves. Evens et al. (Ref 32) proposed a friction correction method as shown in Eq 4 based on Mises yield criterion which well suited the isothermal compression tests (Ref 12, 33, 34).

$$\sigma = \frac{\bar{\sigma}}{1 + (2/3\sqrt{3})m(r_0/h_0) \exp(3\bar{\epsilon}/2)} \quad (\text{Eq 4})$$

where  $\sigma$  is the corrected stress (MPa),  $\bar{\sigma}$  is the measured stress (MPa),  $\bar{\epsilon}$  is the measured strain,  $r_0$  and  $h_0$  are the radius and height before compression,  $m$  is the friction coefficient, which was generally chosen to be 0.2 (Ref 15).

As a result, the comparison of flow stress before (Ref 35) and after correction are shown in Fig. 2. The temperature rising induced softening increases with the increasing strain rate and decreasing temperature. Besides, after friction correction, the flow stress at all conditions reduced to the value below the measured. After all corrections, all the flow stress shows stronger softening effect with straining.

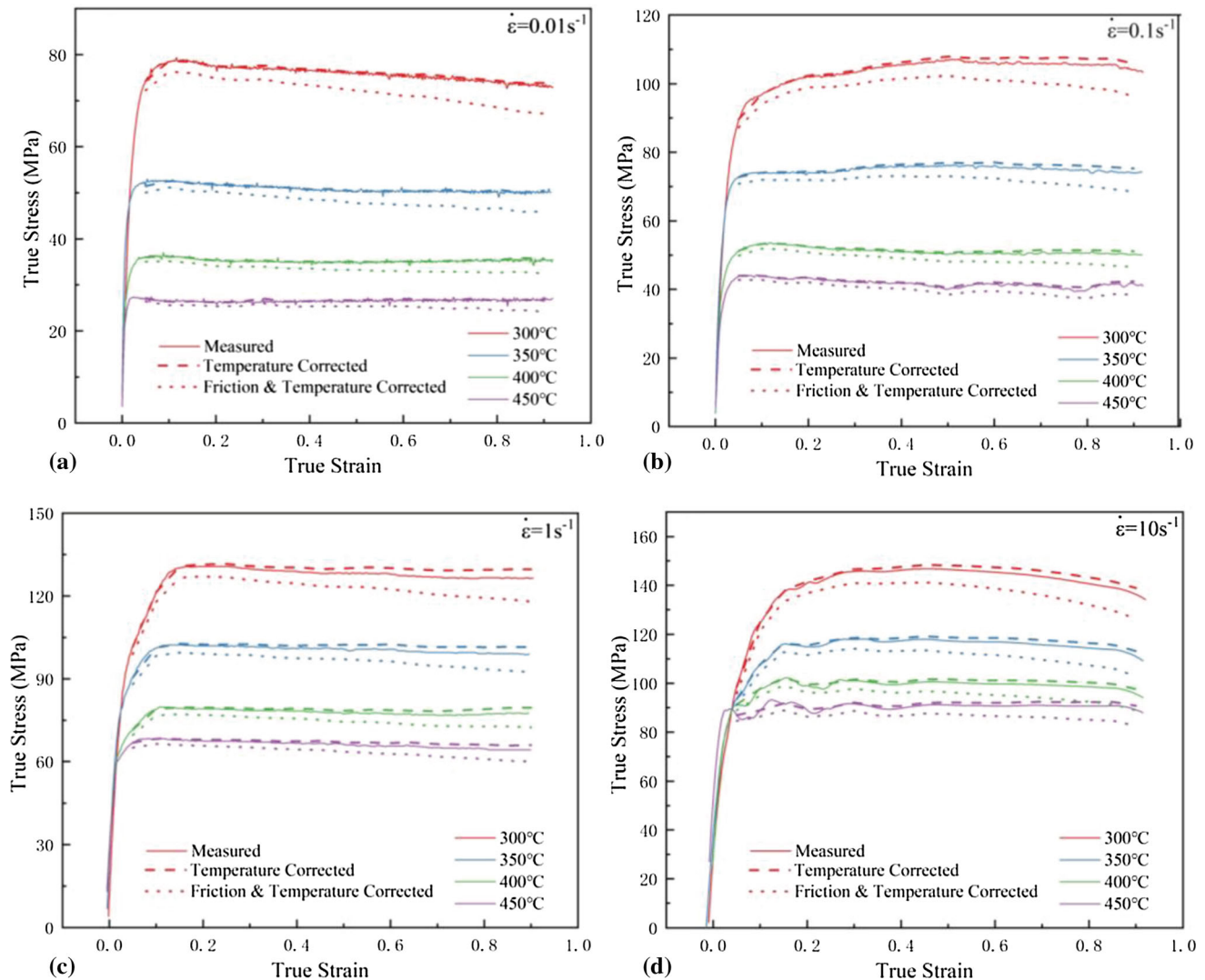


**Fig. 2** The comparison between measure flow stress and corrected flow stress

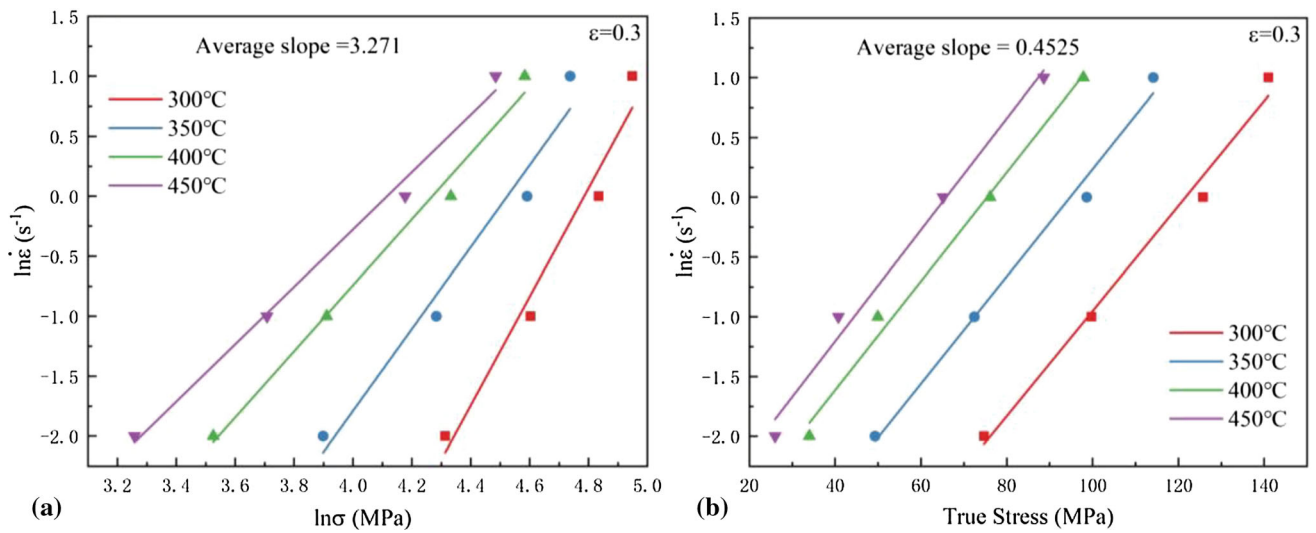


Fig. 3 The linear fitting results of (a)  $\ln \sigma - \ln \dot{\epsilon}$  and (b)  $\sigma - \ln \dot{\epsilon}$  at the strain of 0.3

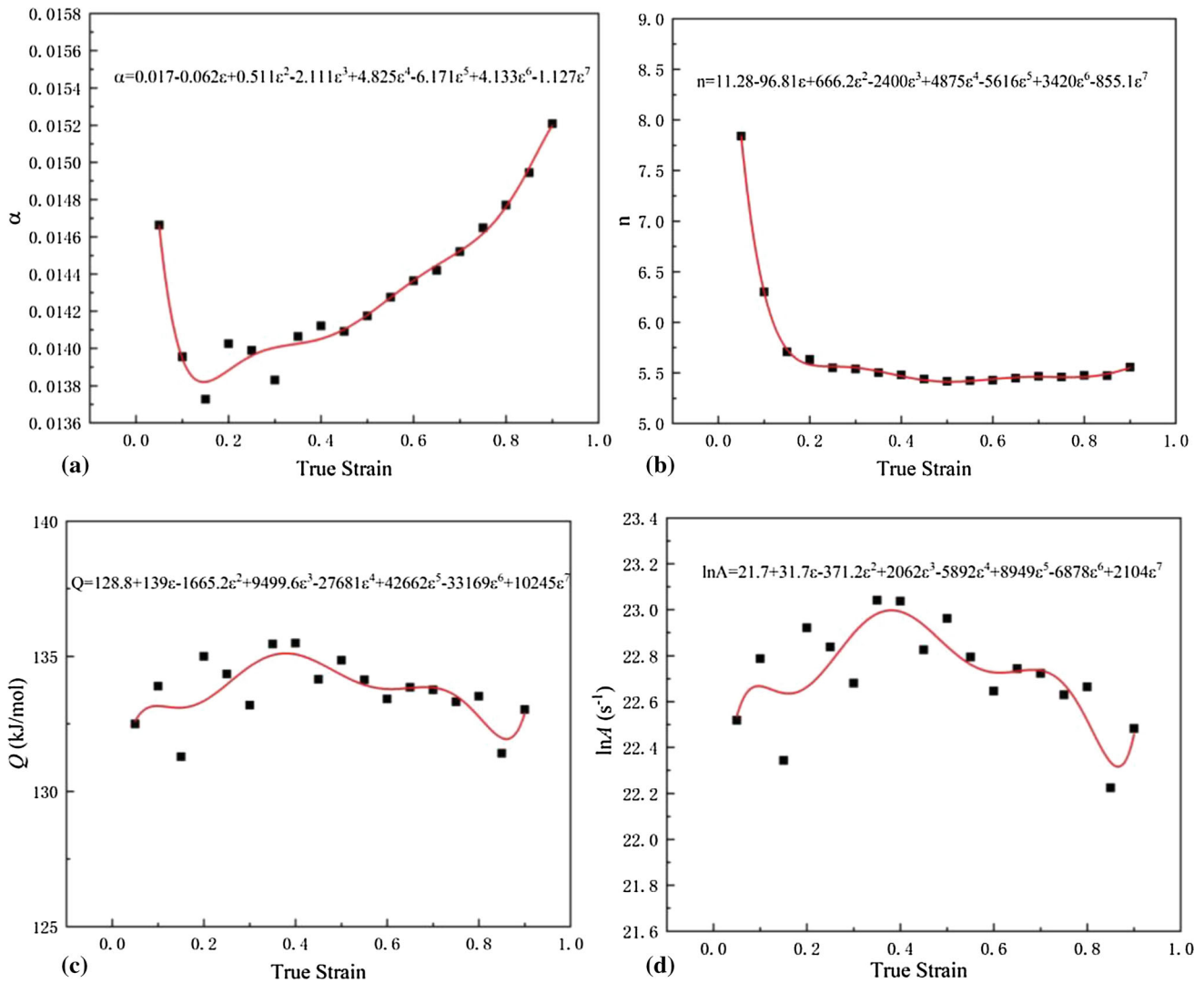


Fig. 4 The 7th ordered polynomial fitting between values of (a)  $\alpha$ , (b)  $n$ , (c)  $Q$ , (d)  $\ln A$  and the strain

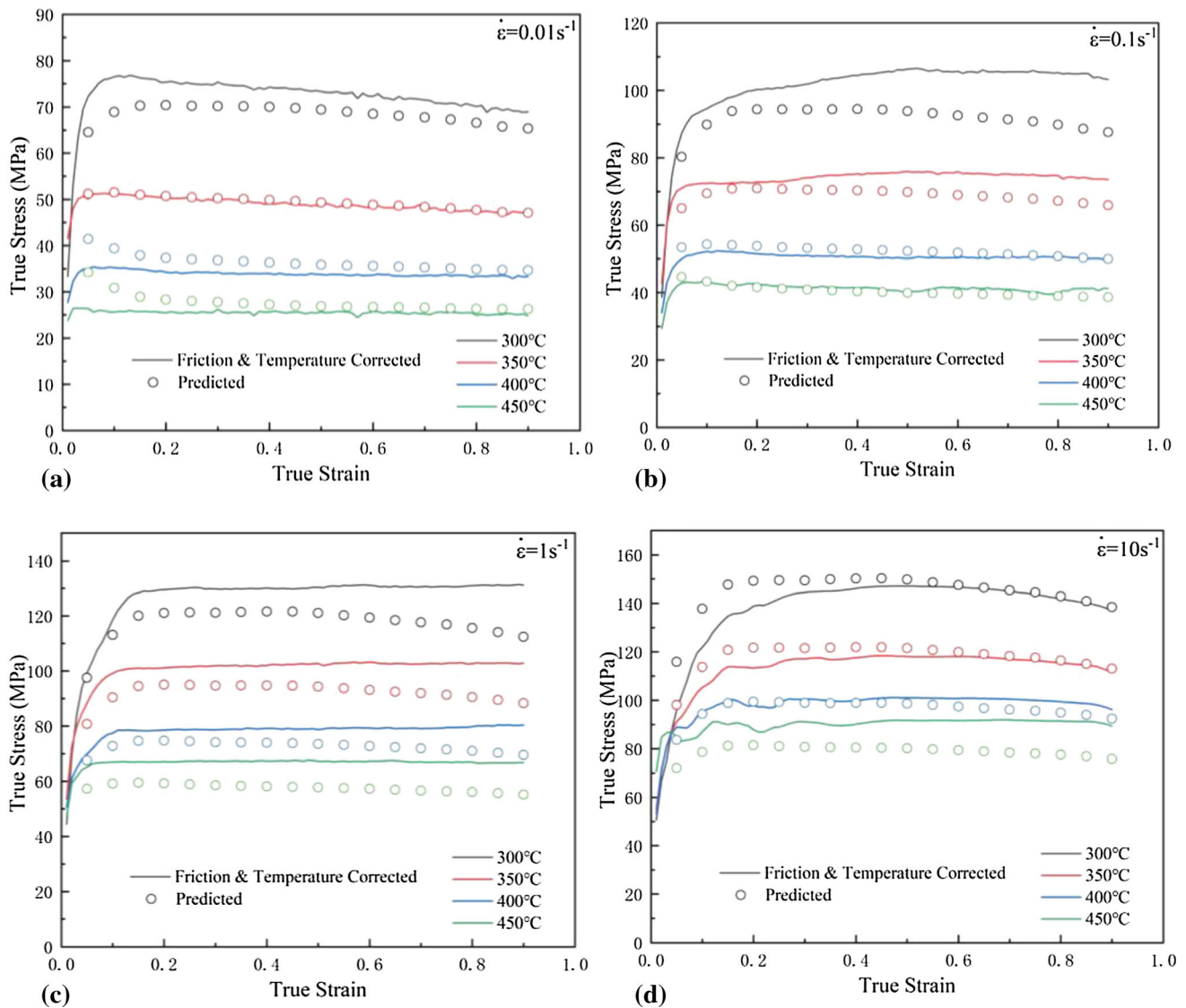


Fig. 5 The comparison between predicted stress and corrected stress

### 3.2 Arrhenius Constitutive Modelling

To describe the constitutive relationship among metals and alloys, the Arrhenius model which contains the following equations has been extensively studied (Ref 19, 36).

$$\dot{\varepsilon} = \begin{cases} A_1 \sigma^{n'} \exp(-Q/RT) \\ A_2 \exp(\beta\sigma) \exp(-Q/RT) \\ A[\sinh(\alpha\sigma)]^n \exp(-Q/RT) \end{cases} \quad (\text{Eq 5})$$

where  $\dot{\varepsilon}$  is the strain rate ( $\text{s}^{-1}$ ),  $Q$  is the deformation activation energy (kJ/mol),  $R$  is gas constant (8.31 kJ/mol/K),  $T$  is the temperature ( $^{\circ}\text{C}$ ),  $\sigma$  is the flow stress (MPa), others are material constants, and  $\alpha = \beta/n'$ .

After taking natural logarithm of both side of Eq 5, it can be expressed as:

$$\ln \dot{\varepsilon} = \begin{cases} \ln A_1 + n' \ln \sigma - Q/RT \\ \ln A_2 + \beta\sigma - Q/RT \\ \ln A + n[\ln \sinh(\alpha\sigma)] - Q/RT \end{cases} \quad (\text{Eq 6})$$

here the values of  $n'$  and  $\beta$  are the average slopes of  $\ln \sigma - \ln \dot{\varepsilon}$  and  $\sigma - \ln \dot{\varepsilon}$  at a certain strain and they can be determined by linear fitting. For example, Fig. 3 shows the linear fitting results of  $\ln \sigma - \ln \dot{\varepsilon}$  and  $\sigma - \ln \dot{\varepsilon}$  at the strain of 0.3 and the values of  $n'$  and  $\beta$  are 3.271 and  $0.4525 \text{ MPa}^{-1}$  respectively, thus the value of  $\alpha$  is  $0.0138 \text{ MPa}^{-1}$ .

After  $\alpha$ -value obtained, the values of  $n$  and  $Q$  can also be calculated according the following equations. Also, linear fitting was used and the values of  $n$  and  $Q$  at the strain of 0.3 were determined to be 5.5775 and 133.99 kJ/mol. After that, the value of  $\ln A$  was determined to be  $22.838 \text{ s}^{-1}$ .

$$n = \frac{\partial \ln \dot{\varepsilon}}{\partial \ln(\sinh(\alpha\sigma))} \Big|_T \quad (\text{Eq 7})$$

$$Q = nR \frac{\partial \ln(\sinh(\alpha\sigma))}{\partial (1/T)} \Big|_{\dot{\varepsilon}} \quad (\text{Eq 8})$$

However, it is not accurate to use the coefficients calculated at a certain strain to predict the flow stress at different strains.

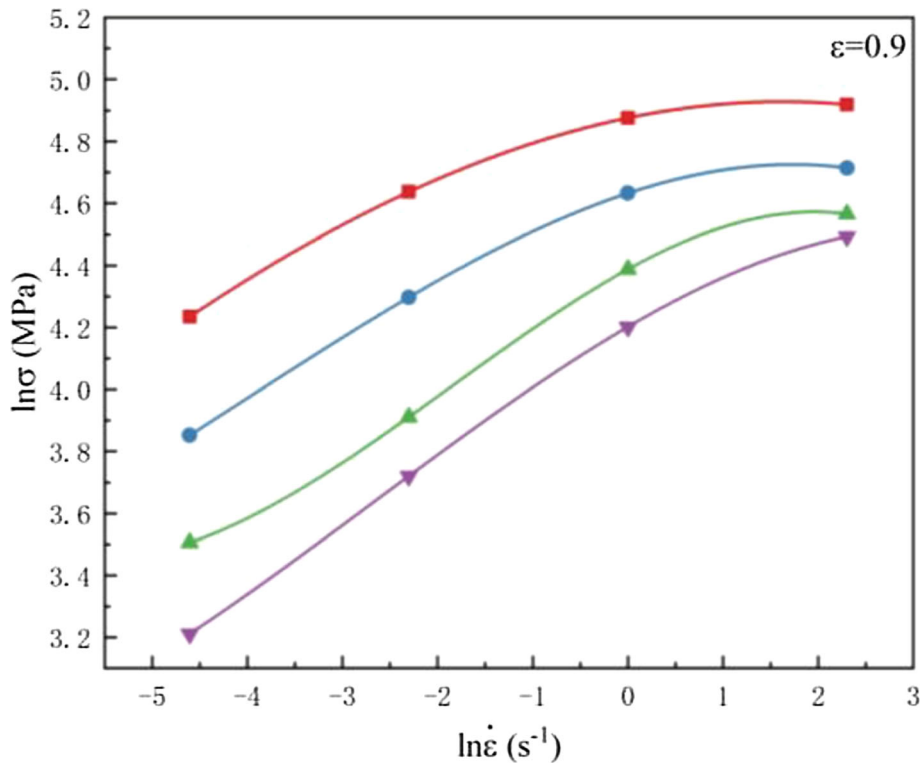


Fig. 6 The third ordered polynomial fitting between  $\ln \sigma - \ln \dot{\epsilon}$  at the strain of 0.9

Table 2 The  $m$ -values at the strain of 0.9

Strain rate, $s^{-1}$	Temperature, $^{\circ}C$			
	300	350	400	450
0.01	0.206	0.196	0.106	0.203
0.1	0.142	0.180	0.218	0.227
1	0.064	0.101	0.169	0.179
10	-0.029	-0.041	-0.041	0.061

Hence, the calculating process above were circularly executed for 18 times from the strain of 0.05-0.9 with an interval of 0.05 to obtain the corresponding values of  $\alpha$ ,  $\ln A$ ,  $n$ ,  $Q$ . Meanwhile, the relationship between the values of  $\alpha$ ,  $\ln A$ ,  $n$ ,  $Q$  and the strain were fitted by 7th ordered polynomial fitting as shown in Fig. 4.

The Zener-Hollomon parameter is generally obtained by Eq 9 and the predicted results can be calculated by Eq 10 (Ref 29, 37). As a result, the comparison between predicted stress and corrected stress are shown in Fig. 5. It can be seen that the predicted stress can accurately describe the flow behavior during hot compression.

$$Z = A [\sinh(\alpha\sigma)]^n = \dot{\epsilon} \exp(Q/RT) \quad (\text{Eq 9})$$

$$\sigma = \frac{1}{\alpha} \left\{ \left( \frac{Z}{A} \right)^{\frac{1}{n}} + \left[ \left( \frac{Z}{A} \right)^{\frac{2}{n}} + 1 \right]^{\frac{1}{2}} \right\} \quad (\text{Eq 10})$$

The prediction precision of the model can be evaluated by correlation coefficient ( $R$ ) and average absolute relative error (AARE) denoted as following equations (Ref 38, 39). The  $R$ -value varies between  $-1$ - $1$ , indicating negative correlation to

positive correlation. Lower AARE-value indicates higher prediction precision. Here, the  $R$ -value and AARE-value were determined to be 0.9841 and 6.2346%, which suggests good prediction accuracy of the strain compensated Arrhenius model.

$$R = \frac{\sum_{i=1}^N (E_i - \bar{E})(P_i - \bar{P})}{\sqrt{\sum_{i=1}^N (E_i - \bar{E})^2 \cdot \sum_{i=1}^N (P_i - \bar{P})^2}} \quad (\text{Eq 11})$$

$$\text{AARE}(\%) = \frac{1}{N} \sum_{i=1}^N \left| \frac{P_i - E_i}{E_i} \right| \times 100\% \quad (\text{Eq 12})$$

where  $E_i$  is the tested value,  $\bar{E}$  is the mean value of tested value,  $P_i$  is the predicted value,  $\bar{P}$  is the mean value of predicted value,  $N$  is the number of values.

### 3.3 Processing Map

It has become a consensus among researchers that processing map unveils the intrinsic workability of alloys under different deformation conditions and it can provide reference for determining optimal hot working window. Before constructing the processing map of this alloy, the strain rate sensitivity index ( $m$ ) at different conditions were calculated according to the Eq 14 which was derived from the third ordered polynomial fitting (Eq 13) between  $\ln \sigma - \ln \dot{\epsilon}$  at a certain strain (Ref 19, 28, 40).

$$\ln \sigma = a_1 + a_2 \ln \dot{\epsilon} + a_3 (\ln \dot{\epsilon})^2 + a_4 (\ln \dot{\epsilon})^3 \quad (\text{Eq 13})$$

$$m = \frac{\partial(\ln \sigma)}{\partial(\ln \dot{\epsilon})} = a_2 + 2a_3 (\ln \dot{\epsilon}) + 3a_4 (\ln \dot{\epsilon})^2 \quad (\text{Eq 14})$$

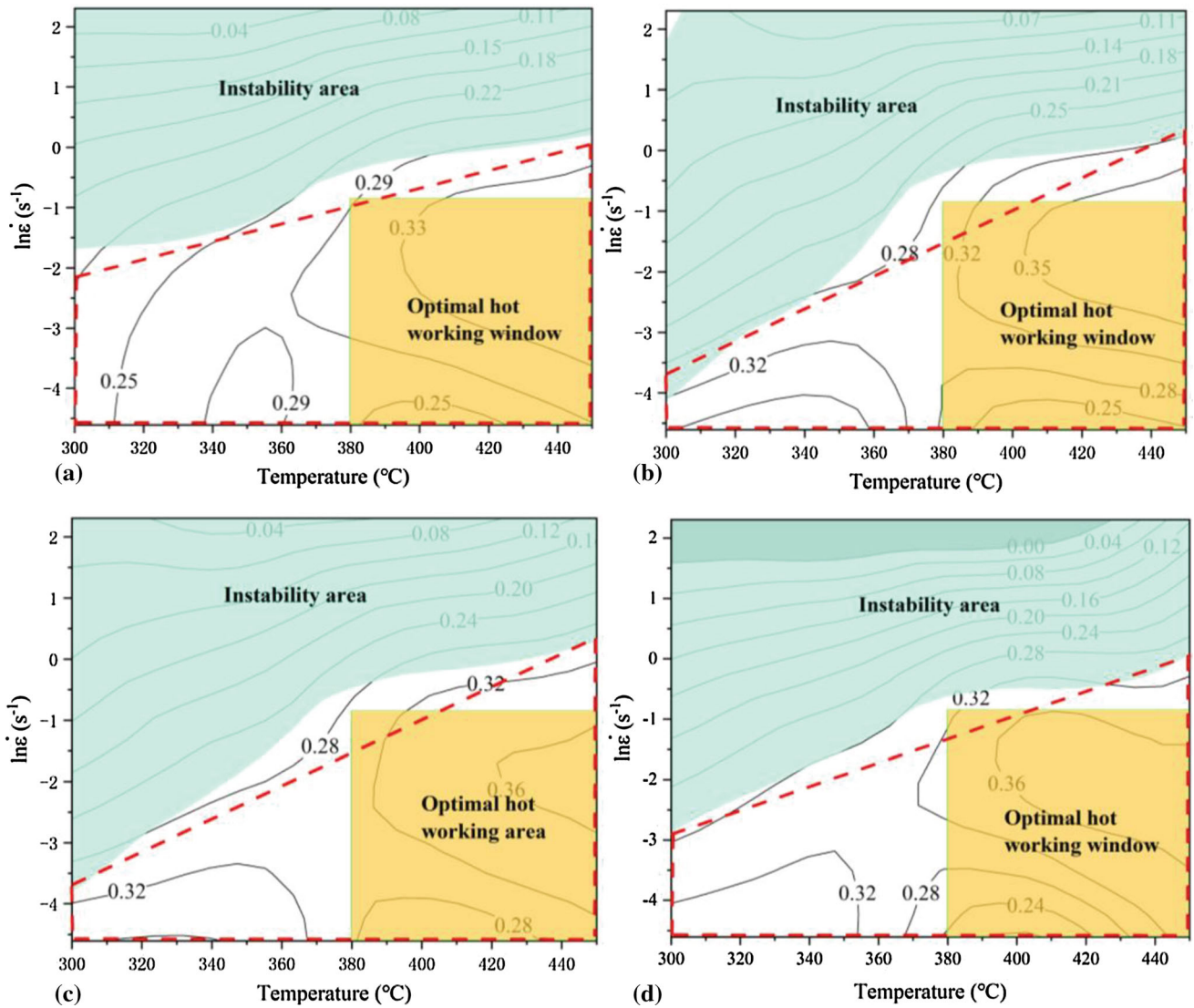


Fig. 7 The processing maps at the strain of (a) 0.3, (b) 0.5, (c) 0.7 and (d) 0.9

where  $a_1$ - $a_4$  are the fitting coefficients obtained by the third ordered polynomial fitting as shown in Fig. 6.

The  $m$ -values for this alloy at the strain of 0.9 were calculated according to Eq 14 after the determination of  $a_1$ - $a_4$  and the results are listed in Table 2. It can be seen that the  $m$ -values varies from  $-0.041$  to  $0.227$ . Negative  $m$ -values at  $300\text{ }^\circ\text{C}$  and  $10\text{ s}^{-1}$  and  $350\text{ }^\circ\text{C}$  and  $10\text{ s}^{-1}$  reveal the occurrence of instable plastic flow and higher  $m$ -values at the region of lower strain rate with higher temperature indicate stable plastic deformation.

The power dissipation efficiency ( $\eta$ ) can be calculated according the simplified equation as shown in Eq 15 proposed by Prasad (Ref 24, 25), which derived from the theory of dynamic materials model.

$$\eta = \frac{2m}{m+1} \quad (\text{Eq 15})$$

Moreover, the instability criterion ( $\zeta$ ) proposed by Prasad (Ref 24) is shown in Eq 16, and it can be derived into Eq 17 for more convenient calculation.

$$\zeta(\dot{\epsilon}) = \frac{\partial \ln \frac{m}{m+1}}{\partial \ln \dot{\epsilon}} + m < 0 \quad (\text{Eq 16})$$

$$\zeta(\dot{\epsilon}) = \frac{\partial m}{\partial \ln \dot{\epsilon}} + m^2 + m^3 < 0 \quad (\text{Eq 17})$$

The processing maps consisting of power dissipation maps and instability maps of this alloy at the strain of 0.3-0.9 are shown in Fig. 7. The labeled number in the contour map are the values of power dissipation efficiency ( $\eta$ -values). Generally, the  $\eta$ -value increases with the increasing temperature and decreasing strain rate. The highest  $\eta$ -value occurs at  $400\text{ }^\circ\text{C}$  and  $0.1\text{ s}^{-1}$  and  $450\text{ }^\circ\text{C}$  and  $0.1\text{ s}^{-1}$ , indicating positive plastic flow operates (DRX or DRV). The cyan areas are the instability regions locating at the areas of strain rate  $> 1\text{ s}^{-1}$  and the regions expand with the decreasing of temperature. The stable regions are in red-dashed trapezoids in Fig. 7. From Fig. 7, it can be concluded that, to tolerate higher strain rate, the hot working temperature needs to keep higher. According to the processing maps, the optimal hot working area of this alloy is

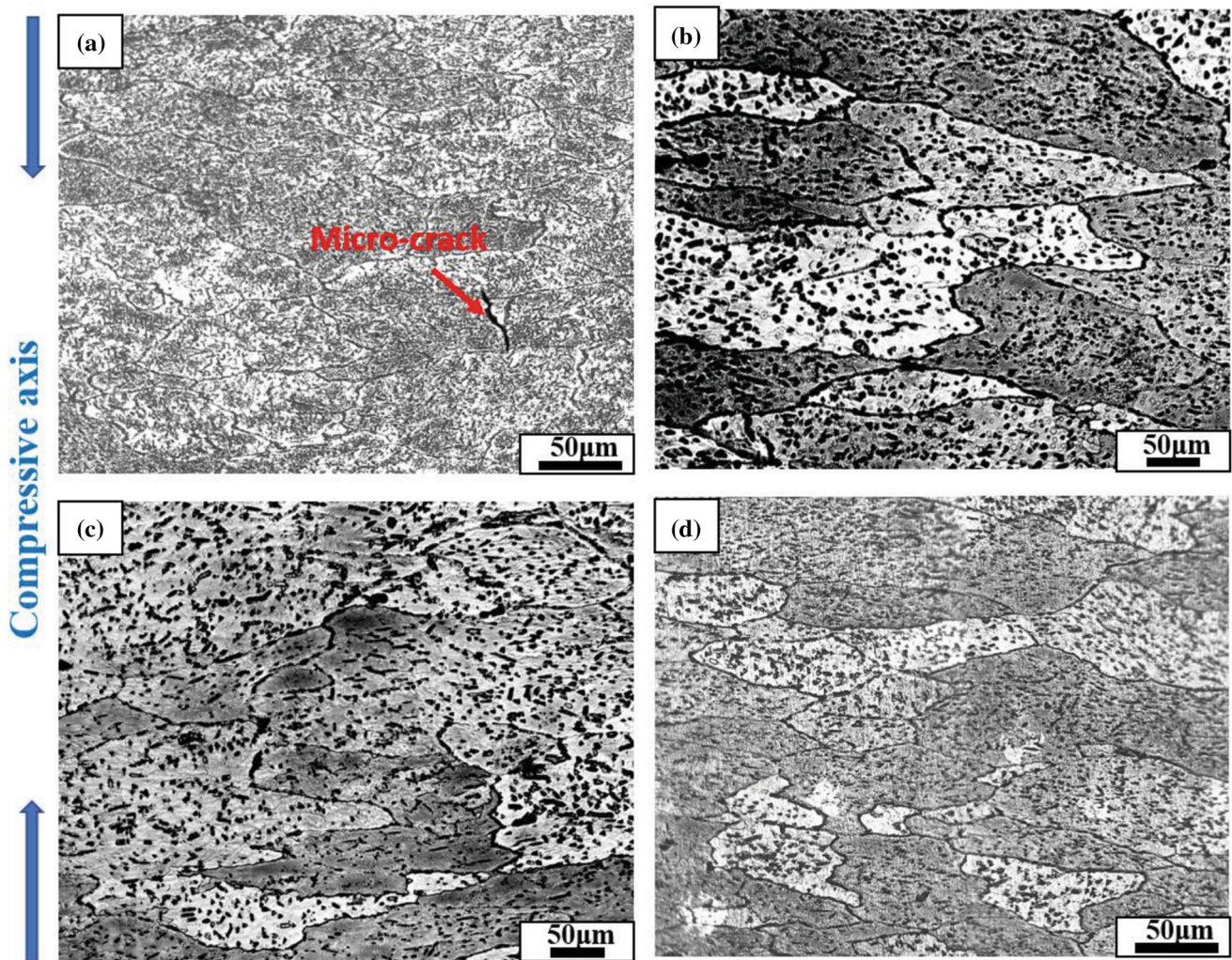


**Fig. 8** The OM microstructures at the conditions of (a) 300 °C and 10 s<sup>-1</sup>, (b) 450 °C and 10 s<sup>-1</sup>, (c) 300 °C and 0.01 s<sup>-1</sup>, (d) 450 °C and 0.01 s<sup>-1</sup>

shown in the yellow rectangular area where temperature > 380 °C and strain rate < 0.368 s<sup>-1</sup> in Fig. 7, where is the stable area with higher  $\eta$ -values.

### 3.4 Microstructure Analysis

The OM microstructures at different deformation conditions are shown in Fig. 8. A micro-crack can be seen at the condition of 300 °C and 10 s<sup>-1</sup> which was identified as an unstable deformation region in Fig. 7. Comparing to Fig. 8(c), under the same temperature with Fig. 8(a) but at lower strain rate of 0.01 s<sup>-1</sup>, the grain boundaries are clearer and the distributions of secondary particles are very different. The particle size of the later one is coarser, which may result from the longer deformation time (0.091 s at the 10 s<sup>-1</sup> and 91 s at 0.01 s<sup>-1</sup>), which offers enough time for the diffusion process. Moreover, the grain size in Fig. 8(a) is obviously smaller than that in Fig. 8(c), the deformation heat induced temperature rising at this condition (300 °C and 10 s<sup>-1</sup>) is about 41.96 °C according to Eq 1, simultaneously, massive dislocations generate, thus the driving force for DRX is increased, resulting in stronger DRX and grain refinement. Figure 8(d) shows the microstructure under 450 °C and 0.01 s<sup>-1</sup>, where is located at the optimal hot working condition with  $\eta$ -value > 0.32 in

Fig. 7, finer and uniform grains can be observed comparing to other conditions. Meanwhile, the secondary phases are finer and more homogeneously distributed.

Figure 9 shows the inverse pole figure (IPF) maps at the temperature of 400 °C with different strain rates. The white thin lines and bold black lines in the IPF maps are low angle grain boundaries (LAGBs, > 2° and < 15°) and high angle grain boundaries (HAGBs, > 15°), respectively. It can be seen that the amounts of LAGBs and HAGBs inside deformed grains increase with increasing strain rate. Besides, typical flow localization marked in red rectangular can be seen in Fig. 9(c) and (d), which corresponds to the instability region in the processing map. Comparing to other three conditions, finer grains in Fig. 9(c) are less, indicating weaker DRX operation, and this results in the weaker softening behavior in flow curves in Fig. 2. In Fig. 9(d), the grain fragment is more pronounced. Higher strain rate is beneficial for the fragmentation of grain due to the formation of dislocation pileups along with higher dislocation multiplication rate. According to Eq 8, the deformation activation energy at 400 °C with strain rates of 0.01 ~ 10 s<sup>-1</sup> are 138.5, 124.9, 121.6 and 111.0 kJ/mol, indicating the deformation process need less heat activation energy to be initiated under higher strain rate. Dislocation pile-



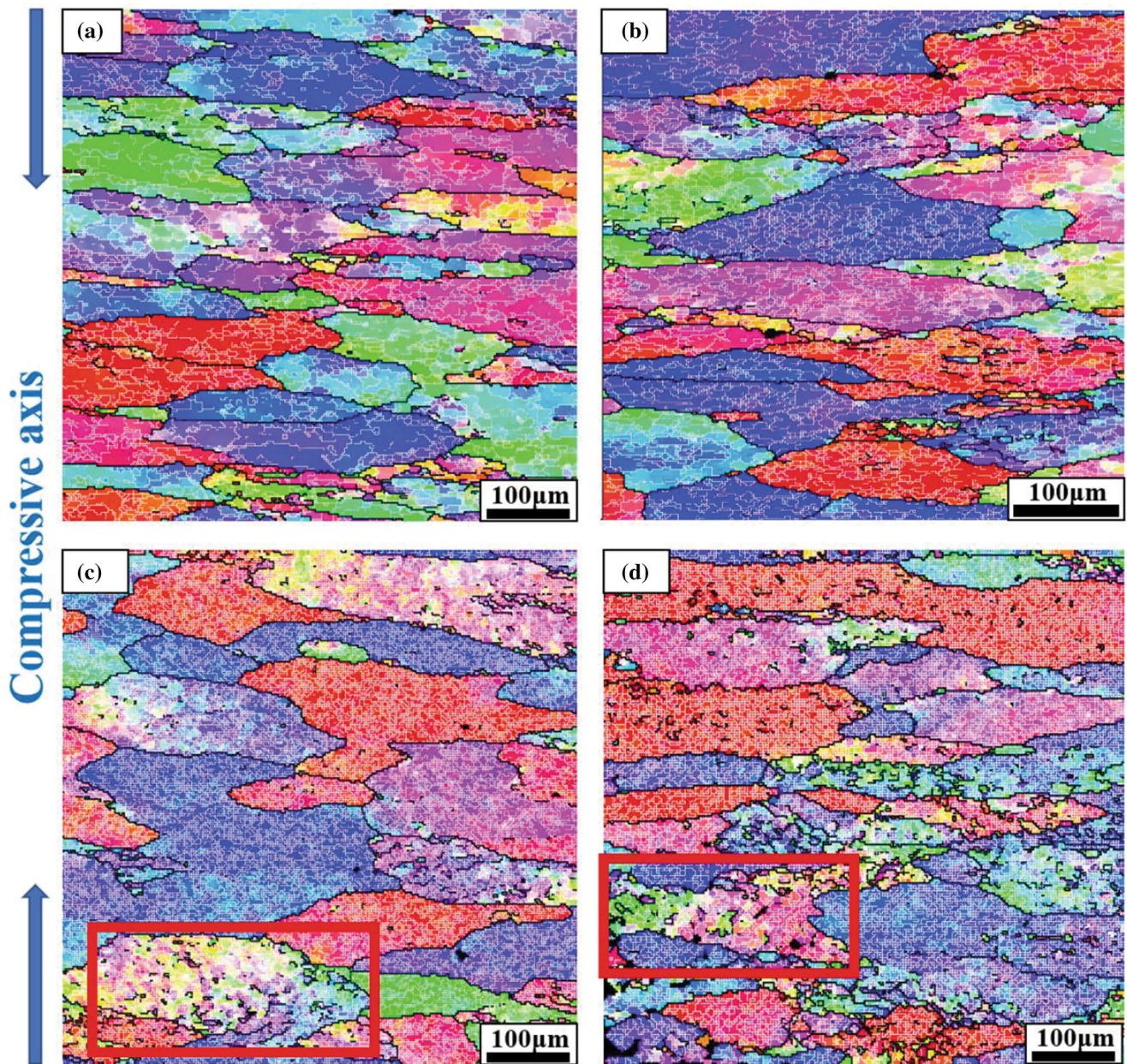


**Fig. 9** The IPF maps at the conditions of (a) 400 °C and 0.01 s<sup>-1</sup>, (b) 400 °C and 0.1 s<sup>-1</sup>, (c) 400 °C and 1 s<sup>-1</sup> and (d) 400 °C and 10 s<sup>-1</sup>

ups and tangles form and promote the formation of subgrains, which results in the increasing of LAGBs. In this process, most of the secondary particles play a positive role for the multiplication of dislocations by hindering its motion. After reaching a critical dislocation density, the DRX predominates, promoting the transformation of LAGBs → HAGBs. Thus, the LAGBs and HAGBs are pronouncedly increased with the increasing strain rate.

In addition to the strain rate, temperature also violently affects the microstructure evolution. Figure 10 shows the DRX distribution maps at the strain rate of 0.1 s<sup>-1</sup> with 350, 400 and 450 °C. The volume fractions of DRX are 36.4, 19.7 and 46.5% under different temperature, respectively. This value is not monotone increasing or decreasing with temperature. On

contrary, it drops to a bottom value at the middle temperature of 400 °C. At the temperature of 350 °C, dislocation multiplication is more efficient, which is easier to break through the critical dislocation density for the initiation of DRX. With the increasing temperature, the diffusion efficiency is promoted, the dislocation multiplication is hindered, which decreases the dislocation density, as well as the driving force of DRX. At higher temperature of 450 °C, due to stronger diffusion efficiency, the driving force for rotation of subgrains and grain boundary migration is enhanced, thus DRX were promoted. The following conditions are all identified to be stable area in processing maps, meanwhile, with  $\eta$ -values approximately higher than 0.3, verified the prediction accuracy.

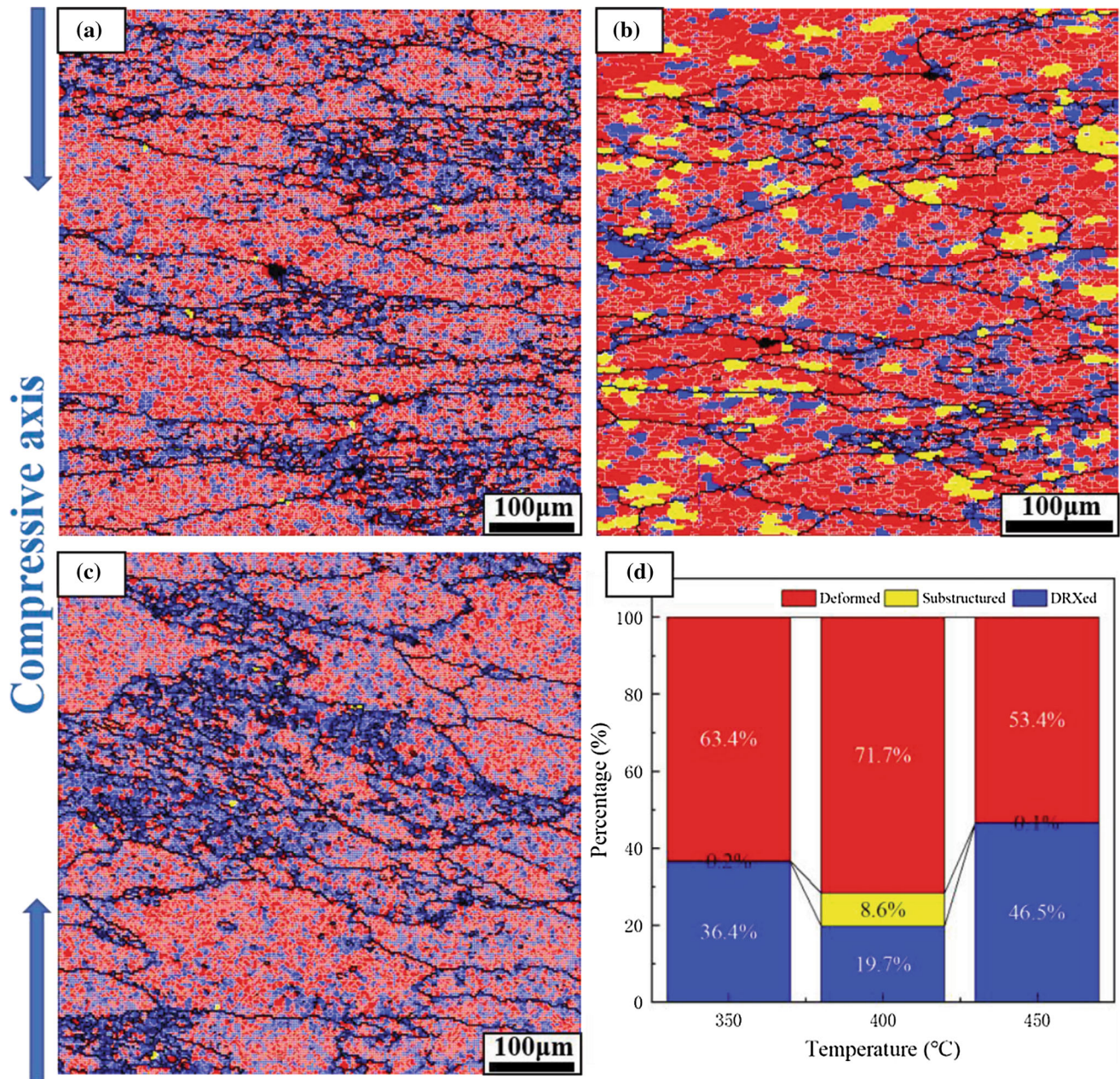


**Fig. 10** The DRX distribution maps at the strain rate of  $0.1 \text{ s}^{-1}$  with (a) 350 °C, (b) 400 °C, (c) 450 °C, and (d) the volume fractions under different conditions

#### 4. Conclusions

The hot deformation behavior of a novel homogenized Al-7.8Zn-1.65Mg-2.0Cu (wt.%) alloy was studied in terms of correction of stress-strain curves, constitutive modelling, processing map development and microstructure evolution analysis through isothermal compression tests and OM/EBSD characterizations. The following conclusions can be obtained:

- (1) Deformation heat-induced temperature rising and friction appreciably influence the flow stress of this alloy, it is necessary to conduct correction before constitutive modelling. The strain compensated Arrhenius model can accurately predict the corrected flow stress with the  $R$ -value of 0.9841 and AARE-value of 6.2346%.
- (2) The  $\eta$ -value of processing map increases with the increasing temperature and decreasing strain rate. It reaches peak in the range of 380-450 °C and  $0.01$ - $0.368 \text{ s}^{-1}$ , where can be identified to be the optimal hot working window. Micro-cracking was observed at 300 °C and  $10 \text{ s}^{-1}$  and flow localization was observed at 400 °C and  $1 \text{ s}^{-1}$  and 400 °C and  $10 \text{ s}^{-1}$ , verifying the instability prediction of processing map.
- (3) The microstructure evolution and flow behavior of this alloy is sensitive to strain rate. The increasing strain rate decreases the deformation activation energy and increases the dislocation multiplication rate, meanwhile, it promotes the formation of subgrains and increasing of LAGBs and HAGBs.

## Acknowledgments

The authors gratefully appreciate Chongqing Science and Technology Commission (cstc2021jcyj-msxmX0653), the Foundation of Science and Technology Project of Chongqing Education Commission (No. KJQN202101515), Research Foundation of Chongqing University of Science and Technology (No. ckr-c2020015), Innovation Research Group of Universities in Chongqing (CXQT21030), Chongqing Talent Project (CQYC201905100).

## Data Availability

The raw/processed data required to reproduce these findings cannot be shared at this time as the data also forms part of an ongoing study.

## Conflict of interest

We declare that we do not have any commercial or associative interest that represents a conflict of interest in connection with the work submitted.

## References

1. M.A. Moazam and M. Honarpisheh, Improving the Mechanical Properties and Reducing the Residual Stresses of AA7075 by Combination of Cyclic Close Die Forging and Precipitation Hardening, *Proc. Inst. Mech. Eng. Part L J. Mater. Des. Appl.*, 2021, **235**(3), p 542–549.
2. F. Chen, H. Qu, W. Wu, J.-H. Zheng, S. Qu, Y. Han, and K. Zheng, A Physical-Based Plane Stress Constitutive Model for High Strength AA7075 under Hot Forming Conditions, *Metals*, 2021, **11**(2), p 314.
3. L.Z. Xu, L.H. Zhan, Y.Q. Xu, C.H. Liu, and M.H. Huang, Thermo-mechanical Pretreatment of Al-Zn-Mg-Cu Alloy to Improve Formability and Performance during Creep-Age Forming, *J. Mater. Process. Technol.*, 2021, **293**, p 117089.
4. G.-Z. Quan, J. Liu, A. Mao, B. Liu, and J.-S. Zhang, A Characterization for the Hot Flow Behaviors of As-extruded 7050 Aluminum Alloy, *High Temp. Mater. Process. (London)*, 2015, **34**(7), p 643–650.
5. J. Li, F.G. Li, J. Cai, R.T. Wang, Z.W. Yuan, and F.M. Xue, Flow Behavior Modeling of the 7050 Aluminum Alloy at Elevated Temperatures Considering the Compensation of Strain, *Mater. Des.*, 2012, **42**, p 369–377.
6. Y. Sun, L. Bao, and Y. Duan, Hot Compressive Deformation Behaviour and Constitutive Equations of Mg-Pb-Al-1B-0.4Sc Alloy, *Philos. Mag.*, 2021, **101**(22), p 2355–2376.
7. M. Bambach, I. Sizova, J. Szynlder, J. Bennett, G. Hyatt, J. Cao, T. Papke, and M. Merklein, On the Hot Deformation Behavior of Ti-6Al-4V Made by Additive Manufacturing, *J. Mater. Process. Technol.*, 2021, **288**, p 116840.
8. J. Tang, J.H. Wang, J. Teng, G. Wang, D.F. Fu, H. Zhang, and F.L. Jiang, Effect of Zn Content on the Dynamic Softening of Al-Zn-Mg-Cu Alloys during Hot Compression Deformation, *Vacuum*, 2021, **184**, p 109941.
9. X.M. Qian, N. Parson, and X.G. Chen, Effects of Mn Addition and Related Mn-Containing Dispersoids on the Hot Deformation Behavior of 6082 Aluminum Alloys, *Mater. Sci. Eng. A-Struct. Mater. Prop. Microstruct. Process.*, 2019, **764**, p 138253.
10. J. Li, X. Wu, L. Cao, B. Liao, Y. Wang, and Q. Liu, Hot Deformation and Dynamic Recrystallization in Al-Mg-Si Alloy, *Mater. Charact.*, 2021, **173**, p 110976.
11. A. Rudra, S. Das, and R. Dasgupta, Constitutive Modeling for Hot Deformation Behavior of Al-5083 + SiC Composite, *J. Mater. Eng. Perform.*, 2018, **28**(1), p 87–99.
12. F. Jiang, J. Tang, D. Fu, J. Huang, and H. Zhang, A Correction to the Stress–Strain Curve during Multistage Hot Deformation of 7150 Aluminum Alloy Using Instantaneous Friction Factors, *J. Mater. Eng. Perform.*, 2018, **27**(6), p 3083–3090.
13. H. Xindi, R. Dong, D. Juan, H. Zong, and L. Zhengfeng, Constitutive Behavior and Novel Characterization of Hot Deformation of Al-Zn-Mg-Cu Aluminum Alloy for Lightweight Traffic, *Materials Research Express*, 2021, **8**(1), p 016532.
14. R.L. Goetz and S.L. Semiatin, The Adiabatic Correction Factor for Deformation Heating during the Uniaxial Compression Test, *J. Mater. Eng. Perform.*, 2001, **10**(6), p 710–717.
15. R. Ebrahimi and A. Najafizadeh, A New Method for Evaluation of Friction in Bulk Metal Forming, *J. Mater. Process. Technol.*, 2004, **152**(2), p 136–143.
16. W. Bao, L. Bao, D. Liu, D. Qu, Z. Kong, M. Peng, and Y. Duan, Constitutive Equations, Processing Maps, and Microstructures of Pb-Mg-Al-B-0.4Y Alloy under Hot Compression, *J. Mater. Eng. Perform.*, 2020, **29**(1), p 607–619.
17. Y. Duan, L. Ma, H. Qi, R. Li, and P. Li, Developed Constitutive Models, Processing Maps and Microstructural Evolution of Pb-Mg-10Al-0.5B Alloy, *Mater. Charact.*, 2017, **129**, p 353–366.
18. Y. Duan, P. Li, L. Ma, and R. Li, Dynamic Recrystallization and Processing Map of Pb-30Mg-9Al-1B Alloy during Hot Compression, *Metall. Mater. Trans. A*, 2017, **48**(7), p 3419–3431.
19. S. Long, Y.-F. Xia, P. Wang, Y.-T. Zhou, F.-J. Gong-ye, J. Zhou, J.-S. Zhang, and M.-L. Cui, Constitutive Modelling, Dynamic Globalization Behavior and Processing Map for Ti-6Cr-5Mo-5V-4Al Alloy during Hot Deformation, *J. Alloy. Compd.*, 2019, **796**, p 65–76.
20. R.Y. Li, Y.H. Duan, L.S. Ma, and S. Chen, Flow Behavior, Dynamic Recrystallization and Processing Map of Mg-20Pb-1.6Al-0.4B Alloy, *J. Mater. Eng. Perform.*, 2017, **26**(5), p 2439–2451.
21. Z. He, Z. Wang, and P. Lin, A Comparative Study on Arrhenius and Johnson-Cook Constitutive Models for High-Temperature Deformation of Ti2AlNb-Based Alloys, *Metals*, 2019, **9**(2), p 123.
22. J. Li, F.G. Li, J. Cai, R.T. Wang, Z.W. Yuan, and G.L. Ji, Comparative Investigation on the Modified Zerilli-Armstrong Model and Arrhenius-Type Model to Predict the Elevated-Temperature Flow Behaviour of 7050 Aluminium Alloy, *Comput. Mater. Sci.*, 2013, **71**, p 56–65.
23. D. Samantaray, S. Mandal, and A.K. Bhaduri, A Comparative Study on Johnson Cook, Modified Zerilli-Armstrong and Arrhenius-Type Constitutive Models to Predict Elevated Temperature Flow Behaviour in Modified 9Cr-1Mo Steel, *Comput. Mater. Sci.*, 2009, **47**(2), p 568–576.
24. Y. Prasad and T. Seshacharyulu, Modelling of Hot Deformation for Microstructural Control, *Int. Mater. Rev.*, 1998, **43**(6), p 243–258.
25. Y.V.R.K. Prasad, H.L. Gegel, S.M. Doraivelu, J.C. Malas, J.T. Morgan, K.A. Lark, and R. Barker, Modeling of Dynamic Material Behavior in Hot Deformation: Forging of Ti-6242, *Metall. Trans. A*, 1984, **15**(10), p 1883–1892.
26. Y.W. Xiao, Y.C. Lin, Y.Q. Jiang, X.Y. Zhang, G.D. Pang, D. Wang, and K.C. Zhou, A dislocation Density-Based Model and Processing Maps of Ti-55511 Alloy with Bimodal Microstructures during Hot Compression in Alpha Plus Beta Region, *Mater. Sci. Eng. A*, 2020, **790**, p 139692.
27. B.N. Sahoo and S.K. Panigrahi, Deformation Behavior and Processing Map Development of AZ91 Mg Alloy with and without Addition of Hybrid In-Situ TiC+TiB2 Reinforcement, *J. Alloy. Compd.*, 2019, **776**, p 865–882.
28. Z. Liang, Q. Zhang, L. Niu, and W. Luo, Hot Deformation Behavior and Processing Maps of As-Cast Hypoeutectic Al-Si-Mg Alloy, *J. Mater. Eng. Perform.*, 2019, **28**(8), p 4871–4881.
29. Y.F. Xia, S. Long, T.-Y. Wang, and J. Zhao, A Study at the Workability of Ultra-High Strength Steel Sheet by Processing Maps on the Basis of DMM, *High Temp. Mater. Process. (London)*, 2017, **36**(7), p 657–667.
30. L.-C. Pu, H.-M. Deng, and T.-Q. Zhang, Numerical Simulation of Temperature and Thermal Stress Field in Quenched 7050 Aluminum Alloy Specimen, *Spec. Cast. Nonferr. Alloys*, 2014, **34**(01), p 29–31.
31. A. Gholamzadeh, and A.K. Taheri, The Prediction of Hot Flow Behavior of Al-6%Mg Alloy, *Mech. Res. Commun.*, 2009, **36**(2), p 252–259.
32. R.W. Evans, and P.J. Scharming, Axisymmetric Compression Test and Hot Working Properties of Alloys, *Mater. Sci. Technol.*, 2001, **17**(8), p 995–1004.
33. V. Singh, C. Mondal, A. Kumar, P.P. Bhattacharjee, and P. Ghosal, High Temperature Compressive Flow Behavior and Associated Microstructural Development in a  $\beta$ -Stabilized High Nb-Containing  $\gamma$ -TiAl Based Alloy, *J. Alloy. Compd.*, 2019, **788**, p 573–585.

34. A. Hajari, M. Morakabati, S.M. Abbasi, and H. Badri, Constitutive Modeling for High-Temperature Flow Behavior of Ti-6242S Alloy, *Mater. Sci. Eng. A*, 2017, **681**, p 103–113.
35. D. Wu, S. Long, S. Wang, S.-S. Li, and Y.-T. Zhou, Constitutive Modelling with a Novel Two-Step Optimization for an Al-Zn-Mg-Cu Alloy and its Application in FEA, *Mater. Res. Exp.*, 2021, **8**(11), p 116511.
36. L.A. Peterson, M.F. Horstemeyer, T.E. Lacy, and R.D. Moser, Experimental Characterization and Constitutive Modeling of an Aluminum 7085-T711 Alloy under Large Deformations at Varying Strain Rates, Stress States, and Temperatures, *Mech. Mater.*, 2020, **151**, p 103602.
37. C. Zener, and J.H. Hollomon, Effect of Strain Rate Upon Plastic Flow of Steel, *J. Appl. Phys.*, 1944, **15**(1), p 22–32.
38. G.-Z. Quan, J. Pan, and X. Wang, Prediction of the Hot Compressive Deformation Behavior for Superalloy Nimonic 80A by BP-ANN Model, *Appl. Sci.*, 2016, **6**(3), p 66.
39. G.Z. Quan, T. Wang, Y.L. Li, Z.Y. Zhan, and Y.F. Xia, Artificial Neural Network Modeling to Evaluate the Dynamic Flow Stress of 7050 Aluminum Alloy, *J. Mater. Eng. Perform.*, 2016, **25**(2), p 553–564.
40. F. Kang, S. Wei, J. Zhang, E. Wang, D. Fan, and S. Wang, Hot Processing Maps and Microstructural Characteristics of A357 Alloy, *J. Mater. Eng. Perform.*, 2020, **29**(11), p 7352–7360.

**Publisher's Note** Springer Nature remains neutral with regard to jurisdictional claims in published maps and institutional affiliations.